Plasticity induced by nanoindentation in a CrCoNi medium-entropy alloy studied by accurate electron channeling contrast imaging revealing dislocation-low angle grain boundary interactions

Frederic Habiyaremye, Antoine Guitton, Florian Schäfer, Felicitas Scholz, Mike Schneider, Jan Frenzel, Guillaume Laplanche, Nabila Maloufi

Plasticity induced by nanoindentation in a CrCoNi medium-entropy alloy studied by accurate electron channeling contrast imaging revealing dislocation-low angle grain boundary interactions

Frederic HABIYAREMYE[a], Antoine GUITTON[a,b,*], Florian SCHÄFER[c], Felicitas SCHOLZ[d], Mike SCHNEIDER[d], Jan FRENZEL[d], Guillaume LAPLANCHE[d], Nabila MALOUFI[a,b,*]

[a]Université de Lorraine–CNRS–Arts et Métiers–LEM3, 57070 Metz, France

[b]Labex Damas–Université de Lorraine, 57073 Metz, France.

[c]Department Materials Science and Engineering, Saarland University, 66123 Saarbruecken, Germany.

[d]Institut für Werkstoffe, Ruhr-Universität Bochum, Universitätsstr. 150, 44801 Bochum, Germany.

*corresponding authors: nabila.maloufi@univ-lorraine.fr

antoine.guitton@univ-lorraine.fr

Abstract

In the present work, interactions of nanoindentation-induced dislocations (NIDs) with a low-angle grain boundary (LAGB) are investigated in a single-crystalline CrCoNi medium-entropy alloy (MEA). Microstructural evolutions before and after nanoindentation were examined using accurate electron channeling contrast imaging. In the as-grown state, the alloy microstructure consists of subgrains separated by LAGBs. After nanoindentation on the (001) plane far away from LAGBs, the load-displacement curves exhibit the typical behavior of metals and alloys with a pop-in marking the elastic-plastic transition. This pop-in is related to the nucleation of NIDs that are observed to form pile-ups on {111} planes. In contrast, when indents are performed in the vicinity of a LAGB with a low misorientation angle of 0.24° and consisting of dislocations spaced ~60 nm apart, different micromechanical responses and deformation mechanisms are observed depending on the distance between the LAGB and the nanoindenter tip. When the distance between the LAGB and the nanoindenter tip is larger than four times the size of the indent (corresponding ratio: $R > 4$), the LAGB does not affect the micromechanical response nor interact with NIDs. In contrast, when the indenter comes in direct or indirect contact with the LAGB ($R < 1$), the load-displacement curve deviates at low loads from the elastic stage, and pop-ins are not observed. In this case, the continuous deformation is accommodated by the movement of the pre-existing LAGB dislocations. For intermediate cases with $1 < R < 4$, the load of the initial pop-in is dependent on the local defect density. In this latter case, the pile-ups of NIDs directly impinge on the LAGB. Microstructural analyses reveal that the LAGB accommodates plasticity by blocking the NIDs, activating a

dislocation nucleation site in the adjacent subgrain/emission of dislocation from the LAGB, and inducing slight motions of its constituent dislocations.

Keywords: dislocations, low-angle grain boundary, NiCoCr medium-entropy alloy, A-ECCI, nanoindentation.

1. Introduction

Medium-entropy alloys (MEAs) and high-entropy alloys (HEAs) consist of two to four and at least five elements, respectively, with nearly equiatomic concentrations [1-2]. Among these new classes of materials, the CrMnFeCoNi HEA and one of its equiatomic ternary derivatives, the CrCoNi MEA, are currently receiving increasing interest in the literature [3-4,5] because they both exhibit outstanding damage tolerances at 77 K and 293 K with CrCoNi showing superior properties. This alloy possesses an exceptional combination of tensile strength (1.3 GPa), ductility (up to 90%), and fracture toughness (275 $MPa \cdot m^{-1/2}$) at 77 K [6], even superior to that of high-end cryogenic high Ni-steels [7]. This makes the equiatomic CrCoNi MEA a promising alloy for low-temperature applications [8].

Some of the reasons for the outstanding damage tolerance of the CrCoNi MEA are low stacking fault (SF) energy (22 ± 4 $mJ \cdot m^{-2}$ [9]) and high shear modulus [10] that promote strong work hardening rates (*e.g.*, forest hardening is directly proportional to the shear modulus). The low SF energy does not only promote planar glide of dissociated dislocations and hinders cross-slip, but also favors deformation nanotwinning. This latter deformation mechanism introduces coherent interfaces acting as barriers to dislocation motion and results in a dynamic Hall-Petch effect without reducing ductility [6,9,11-12]. From a more

general point of view, the strengthening due to grain boundaries and annealing twin boundaries (Hall-Petch strengthening) in the CrCoNi MEA was reported to be particularly effective with a Hall-Petch slope of 600 $MPa \cdot m^{-1/2}$ [13]. However, even though promising modeling advances were recently reported in the literature [14-15], there is still a lack of understanding regarding the relative contributions of different types of boundaries to the overall yield strength, *i.e.*, interactions of dislocations with different types of boundaries, such as low-angle grain boundaries (LAGB), coherent twin boundaries and general high-angle grain boundaries. In the present study, we investigated LAGB-dislocation interactions in a single-crystalline CrCoNi MEA. This choice is motivated by recent studies of HEAs and MEAs single crystals for which a significant scatter of critical resolved shear stresses (CRSS) was reported in the literature [16-18]. As these alloys are chemically complex and exhibit dendritic solidification, the LAGB density may strongly vary from one study to another depending on the growth rate. As LAGBs resist the motion of dislocations, different LAGB densities are probably responsible for the observed scatter of CRSS values [19]. Therefore, it is important to characterize LAGB-dislocation interactions in MEAs and HEAs to better understand how LAGBs contribute to the strength of MEA and HEA single crystals.

From a more general viewpoint, much of what is known about dislocation-LAGB interactions in pure metals and alloys mainly comes from numerical studies by discrete dislocation dynamics (DDD) and molecular dynamics (MD) [20-24] and sometimes from theoretical studies [25] because experimental investigations are limited due to difficulties related to carrying them out. For example, Kappor and

Verdhan [23] studied the interactions of pile-up dislocations with low angle tilt boundaries in face-centered cubic (FCC) crystals. The authors showed that the interactions occur by collinear annihilation along with Lomer and glissile junction formations [23-24]. Similarly, the formation of symmetric and asymmetric Hirth Locks, as well as direct transmission of dislocations, were found to be the main interactions between dislocations and Lomer-type LAGB in pure Ni using MD simulation [25]. Only a handful of experimental investigations are available and were mainly performed by *in-situ* and *ex-situ* tests inside a transmission electron microscope (TEM). The impediment of motion and trapping of lattice dislocations by the LAGB as well as the emission of dislocations were observed during *in-situ* nanoindentation inside the TEM in $SrTiO_3$ [26] and Fe-0.4wt%C [27]. The LAGBs were also found to act as barriers to dislocation motion and as nucleation sites in martensitic steels during *in-situ* micromechanical testing in the TEM [28]. Further experimental investigations of dislocations-LAGB interactions are important because LAGBs are prevalent in single crystals of metallic materials [29], annealed metals and alloys [30-33], ultrafine-grained materials [34-37], and martensitic steels [28]. They also pave the way for the understanding of intergranular plasticity [38-39].

From a fundamental point of view, the relationship between microstructure evolution and mechanical properties near GBs is not fully understood. Various attempts to bridge such experimental shortages were done by carrying out nanoindentation in the vicinity of GBs, analyzing the micromechanical responses, and theoretically linking them with dislocation activities without any dislocation scale imaging [40-43]. Soiffer et al. [40] found that hardness values increased by

33% in the vicinity of GBs compared to the hardness values inside grains in pure Cu and attributed this behavior to GB steps produced by electropolishing, the anisotropy of dislocation-GB interactions, etc. Later on, the authors linked dislocation transmission across GBs to the initial pop-in event on the load-displacement curve for indents performed between $0.2 < R < 0.4$ (R is the ratio of the distance to the GB to the residual indent size) in a BCC Fe-14wt% Si because they did not observe pop-ins in the matrix (far away from the GBs) [41]. In contrast to these observations, Wang and Ngan [42] observed two large pop-ins when nanoindentation tests were performed close to GBs in pure niobium. They attributed the first and second pop-ins to incipient plasticity and the sudden transmission of dislocations across the GB, respectively. A similar interpretation was also provided by Pöhl [43] who investigated the occurrence of pop-ins in a pure iron polycrystal. However, the author also pointed out that several other mechanisms (see Fig. 8 of Ref. [43]) and factors (surface roughness, initial dislocation density…) could be responsible for strain bursts observed during nanoindentation. Since there are several possibilities to account for the occurrence of strain bursts during nanoindentation, these tests must be accompanied by dislocation-scale observations, which is one of the objectives of the present study. In this context, instrumented nanoindentation is used to locally induce plasticity in the vicinity of a LAGB. Then, accurate electron channeling contrast imaging (A-ECCI) is employed *post mortem* to monitor the resulting microstructural changes. A-ECCI is chosen here because it allows to image and characterize defects such as individual dislocations [44-46], LAGBs [47], SFs [48] in relatively large areas at depths up to ~100 nm below the specimen surface.

Indeed, imaging of dislocation distribution is very crucial for understanding what happens in the vicinity of the LAGB after nanoindentation. For more details about the working principle of A-ECCI, the reader may refer to Refs. [44,49]. The combination of these two techniques, therefore, allows us to examine how nanoindentation-induced dislocations (NIDs) interact with LAGBs and link these interactions to micromechanical responses in an alloy with a low SF energy.

2. Materials and methods

An [001]-oriented single crystal of the $Cr_{33.3}Co_{33.3}Ni_{33.3}$ (at.%) MEA was processed by the seeded Bridgman technique using a CMSX-4 type Ni-base superalloy [10,50]. A cylindrical cross-section with a diameter of 12 mm and a height of 8 mm was cut at 90° from the growth axis. The sample was polished with diamond suspensions down to 1 µm and then subjected to chemo-mechanical polishing in an aqueous solution of hydrogen peroxide mixed with an oxide suspension to obtain a deformation-free surface.

Microstructural characterization was performed using A-ECCI and high-resolution electron backscatter diffraction (HR-EBSD) in a Zeiss AURIGA SEM (Oberkochen, Germany). Note that the sample was not repolished after nanoindentation. The ECC micrographs were acquired using a standard four-quadrant silicon diode backscattered electron (BSE) detector placed under the pole piece using an acceleration voltage of 20 keV, and a 6.1 mm working distance. EBSD maps were acquired with a commercial EBSD system, Aztec (Oxford Instrument, Inc., UK) using the same acceleration voltage and a step size of 0.35 µm. The sample was mounted on a holder pre-tilted at 70° to the

horizontal. Post-processing of the map was carried out using the HKL Channel 5 (Oxford Instrument, Inc., UK) and ATEX [51] (LEM3, France) software packages.

Compositional analyses were carried out using energy-dispersive X-ray spectroscopy (EDX) in an SEM of type JEOL JSM-IT 300 equipped with an Octane Elite EDAX Ametek detector and the analytical software EDAX Genesis (v.6.53). An accelerating voltage of 25 kV in combination with a probe current of 60 mA, a working distance of ~10 mm, and a count rate of ~150.000 counts/s were used. A total number of 1024 frames were collected, resulting in a total recording time of ~10 h.

Local plastic deformation was introduced in the vicinity of a LAGB using a nanoindenter (Hysitron TI-900, Bruker, US) with a Berkovich tip (Synton-MDP AG, Switzerland). The latter is chosen because it is sharp with a small tip radius of less than 200 nm, suitable for placing indents as close as possible to LAGBs [52]. Nanoindents were performed using a load-controlled mode and peak load of 500 µN. They were spaced at least 3 µm apart to avoid any mutual interaction.

3. Results

3.1. Microstructure before nanoindentation

3.1.1. Microstructure overview of the single crystal

The equiatomic CrCoNi MEA crystallizes with a single-phase FCC structure [9]. A representative BSE micrograph (Fig. 1a) of the sample showcases various randomly oriented dendrites with variable sizes (average: ~100 µm) and contrasts. Such a dendritic morphology is also referred to as crystal mosaicity in

192 the literature and was, for example, observed in Ni-base superalloy single crystals
193 grown by the same technique [50,53].

194 An HR-EBSD map was acquired for the area marked with a white frame in Fig. 1a
195 for detailed investigation. The corresponding misorientation map in Fig. 1b
196 reveals that the misorientation angles (θ) between neighboring dendrites can be
197 as small as 0.2° and that most of them are lower than 2°. Therefore, these
198 dendrites are separated by LAGBs since the misorientations are lower than 10°
199 [26]. These dendrites are also referred to as subgrains. To obtain a precise
200 orientation of the subgrain marked with a white frame in Fig. 1b, the procedure
201 reported in Ref. [44] was followed, *i.e.*, a high-resolution selected area channeling
202 patterns (e.g, white frame in Fig. 1c) were recorded at different tilt and rotation
203 angles and superimposed on a simulated Kikuchi pattern for indexing. From the
204 area of the subgrain highlighted with a white frame in Fig. 1b, the ECC
205 micrograph shown in Fig. 1d was acquired with the diffraction vector $\boldsymbol{g} = (2\bar{2}0)$.
206 Figure 1d shows asymmetrical wing-shaped spots with a black and white (B-W)
207 contrast. Each spot corresponds to a trace on the surface of a threading
208 dislocation (TD), *i.e.*, a dislocation nearly perpendicular to the surface. Moreover,
209 there is a highly inclined dislocation that appears with a comet-like contrast (white
210 circle in Fig. 1d). The same area was imaged with $\boldsymbol{g}$ = (220) and a similar number
211 of dislocations were observed.

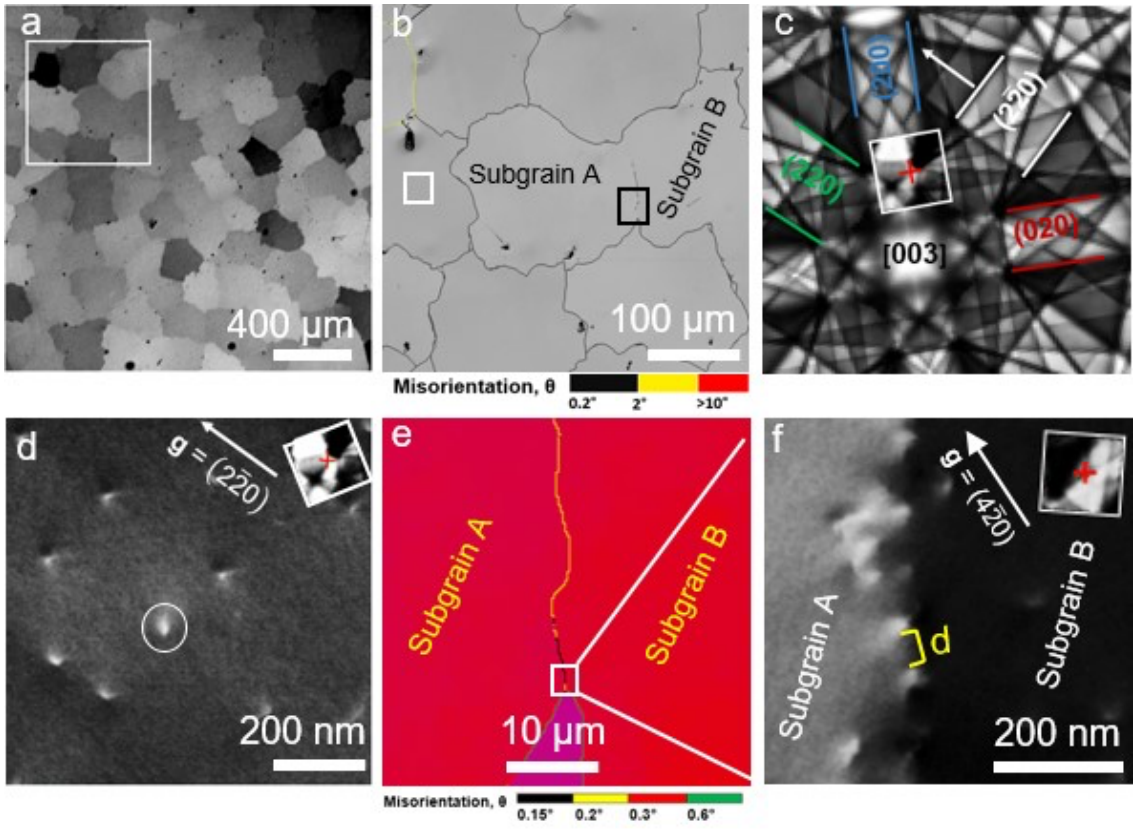

212

213 Fig. 1. (a) BSE micrograph of an [001]-oriented single-crystal of the CrCoNi alloy.
214 (b) Grain boundary misorientation map of the white-framed region in (a). (c) High-
215 resolution selected area channeling pattern (HR-SACP) from the white frame in (b)
216 superimposed onto a simulated Kikuchi pattern where the red cross marks the optical
217 axis of the SEM. (d) ECC micrograph taken inside the subgrain highlighted with a white
218 frame in (b) using $\boldsymbol{g}$ = (2$\bar{2}$0), see white arrow in (c). (e) Grain boundary misorientation
219 map of the black-framed region in (b) superimposed onto a subgrain orientation map.
220 Here, ECC analysis was performed at the region framed in white. (f) ECC micrograph of
221 the LAGB under $\boldsymbol{g}$ = (4$\bar{2}$0). Note that the HR-SACP shown in the upper right corner of (f)
222 is not superimposed onto the simulated Kikuchi pattern in (c) for readability reasons.

223 The TDs offer an advantage over curved or straight dislocations [54] because
224 they allow a better estimation of the dislocation density (ρ) using Eq. (1):

$$\rho = \frac{N}{A} \quad (1),$$

where N is the number of TDs and A is the surface area of the micrograph [47]. The ρ value averaged over 20 micrographs (total area: 140 μm^2) taken inside five different subgrains is $(3.6 \pm 0.9) \times 10^{12}$ m^{-2}. This value is comparable to that found in as-cast single crystals [55].

Figure. 2a shows a BSE micrograph where several subgrains/dendrites can be observed. The EDX maps shown in Figs. 2b-d display the distribution of chemical elements within the dendritic microstructure and the results of EDX point analyses, performed at locations highlighted by the numbers 1-4 in interdendritic and 5-8 in dendritic regions, are summarised in Table 1, respectively. The dendrites are enriched in Co and depleted in Cr with an average composition of $Cr_{30}Co_{36}Ni_{34}$ and have a size of ~100 µm. In contrast, interdendritic regions are ~25 µm wide with an average composition of $Cr_{35}Co_{32}Ni_{33}$.

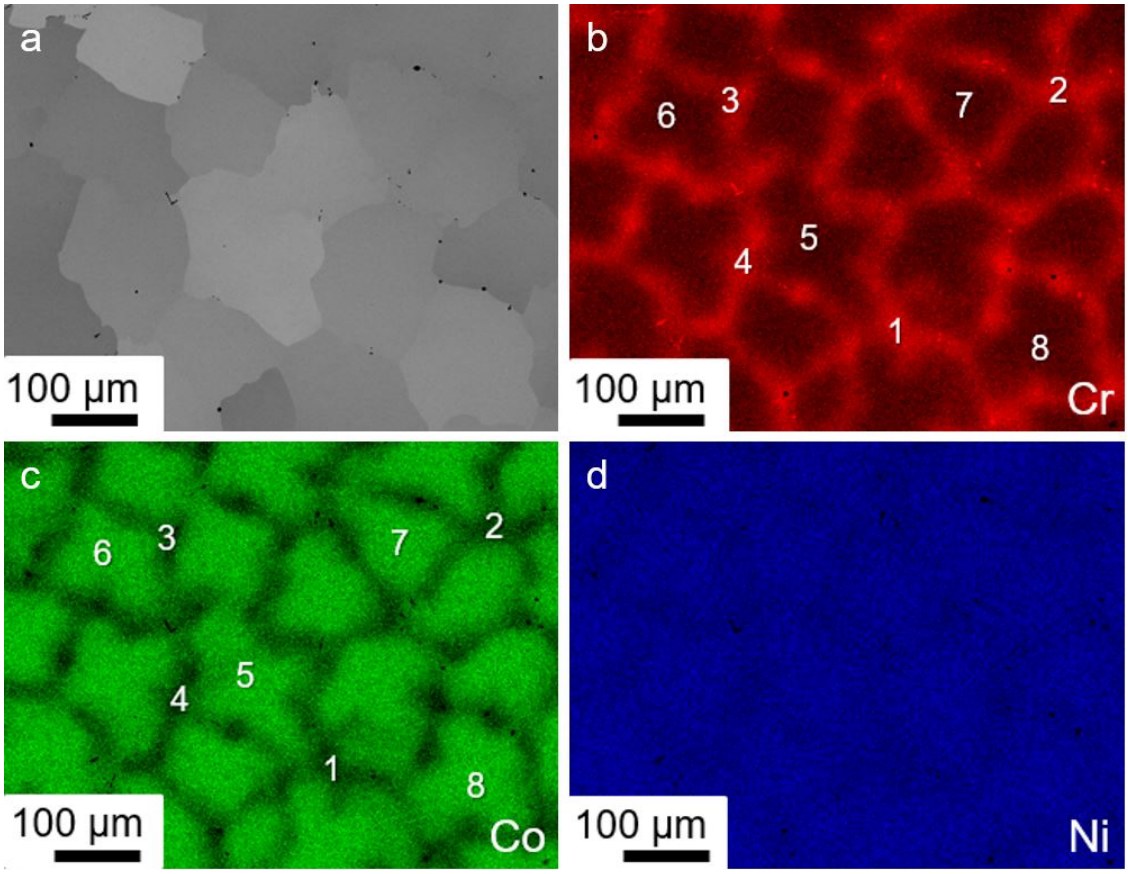

Fig. 2. (a) BSE micrograph of an [001]-oriented single crystal of the CrCoNi alloy. EDS maps of (b) Cr, (c) Co, and (d) Ni.

Table 1. Chemical composition in dendritic and interdendritic regions (in at.%) for positions in Fig. 2c and 2d

Interdendritic regions				Dendritic regions			
N°	Cr	Co	Ni	N°	Cr	Co	Ni
1	35.0	31.5	33.5	5	30.0	36.0	34.0
2	35.0	32.0	33.0	6	30.5	35.5	34.0
3	35.0	31.5	33.5	7	30.0	36.0	34.0
4	35.0	31.5	33.5	8	30.0	35.5	34.0

Since all our nanoindents were performed at distances that are at most 12 µm away from the LAGB (see Fig. 3a), the mechanical responses are therefore representative of the composition present in the interdendritic regions ($Cr_{35}Co_{32}Ni_{33}$).

3.1.2. Structure of the LAGB of interest

The region marked with a black frame in Fig. 1b is magnified in the crystallite orientation map shown in Fig. 1e where the red color indicates that the crystallites have near {001} orientations. Figure 1e is centered on a LAGB of interest that separates subgrains A and B. The range of θ-values along the LAGB is 0.15°-0.3° as deduced from the misorientation map. Assuming that this LAGB consists of an array of equally spaced dislocations, invoking the model of Read and Shockley [55], the expected spacing between dislocations (d) can be estimated using:

$$d = \frac{|\mathbf{b}|}{2\sin(\theta/2)} \quad (2),$$

where $\boldsymbol{b}$ = ½ a <110>. Using θ = 0.15-0.3° in combination with Eq. 2, we find d values between 100 and 50 nm. The ECC micrograph (Fig. 1f) acquired with $\boldsymbol{g} = (4\bar{2}0)$ in the white-framed region of Fig. 1e shows that the LAGB consists of an array of TDs with a mean spacing d = 60 ± 5 nm (see the yellow bracket in Fig. 1f). From this value, an average misorientation of 0.24 ± 0.02° can be deduced from Eq. 2. This latter value is consistent with the misorientation angle determined by EBSD and validates our approach using A-ECCI.

Due to the surface relaxation effect, the Burgers vectors of the TDs within grains in Fig. 1d and along the LAGB in Fig. 1f cannot be determined using the invisibility criteria $\boldsymbol{g} \cdot \boldsymbol{b} = 0$ and $\boldsymbol{g} \cdot \boldsymbol{b} \times \boldsymbol{u} = 0$, where $\boldsymbol{u}$ is a unit vector along the dislocation

line [44-45,56-57] because these dislocations exhibit a residual contrast even if the invisibility criteria are fulfilled. Therefore, it is not straightforward to determine whether a particular dislocation has an edge, mixed, or screw character. However, Tunstall and Hirsch [56] showed by theoretical calculations and TEM imaging in Pt and Cu that the B-W contrast of TDs is stronger and laterally larger for screw TDs than edge TDs. As the TDs along the LAGB (Fig. 1f) show varying contrasts, this implies that the boundary has a mixed tilt and twist character.

3.2. Mechanical response and microstructure after nanoindentation

An array of 56 indents was performed in the vicinity of the LAGB of interest. Among these indents, 15 indents, surrounded by a red line in Fig. 3a, were selected and the load at which the first pop-in was observed on the corresponding load-displacement curves (to be described in Section 3.2.1) was plotted against the distance to the LAGB in Fig. 3b (see *x*-axis at the top) and the normalized distance *R* (ratio between the distance to the LAGB and the indent size, see bottom *x*-axis in Fig. 3b). Since the indent size is ~0.5 μm, *R* is twice the distance to the LAGB. This plot shows that the distribution of pop-in loads is centered around a mean value of 158 μN with a standard deviation of 23 μN when $R > 1$ (black dashed line in Fig. 3b). This distribution can be attributed to the initial local defect density prior to nanoindentation [43]. It also shows that the indents closest to ($R < 1$, #4 and #3 in Fig. 3a) and in contact with the LAGB (#5) exhibit a pop-in at the elastic-plastic transition that is either significantly lower than the mean value (#3) or simply absent (#4 and #5). In addition, two indents (#1 and #2 in Fig. 3a) inside subgrains A and B were investigated.

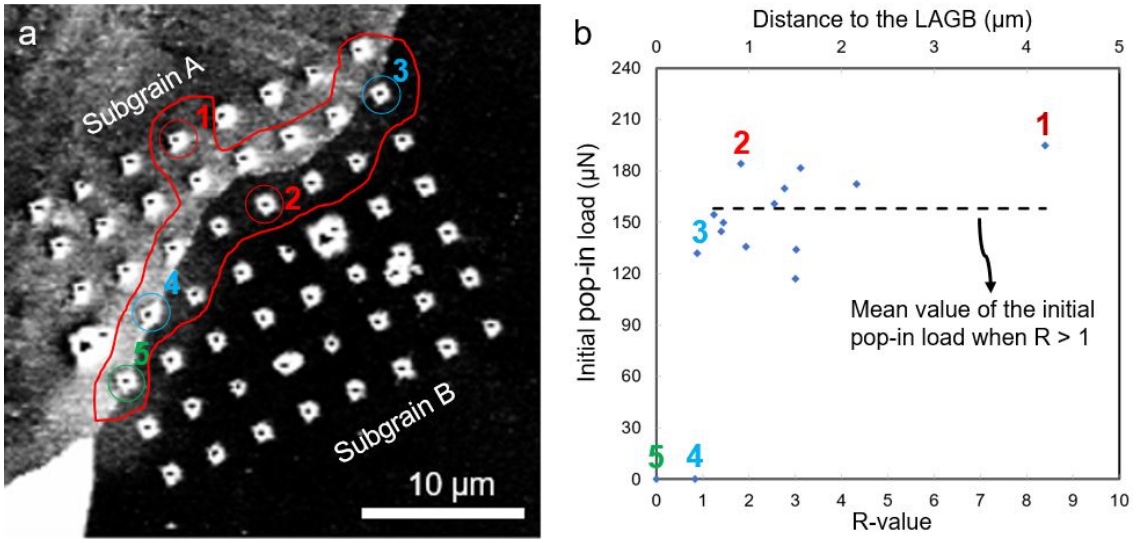

Fig. 3. (a) Array of 7×8 indents around the LAGB. The indents surrounded by the red line and that are close to the LAGB were used to plot the load of the initial pop-in against distance to the LAGB in (b). These distances were also normalized with respect to the size of the remnant indent, see ratio *R* at the bottom *x*-axis of (b). Numbers and colored circles show indents that are analyzed in detail in Section 3.2. The black dashed line in (b) shows the average initial pop-in load of indents when $R > 1$.

These indents were chosen because they show similar low initial dislocation densities and they are far enough from the LAGB such that their local micromechanical responses are not affected. The next sections compare the microstructure evolution and mechanical response of the five above-mentioned indents and the results are presented in Figs. 4-7.

3.2.1. Nanoindentation inside subgrains

We now present the micromechanical responses and microstructural evolutions from the representative indents performed in the interior of the subgrains. Nanoindentation tests were performed in subgrains A and B (indents #1 and #2 shown in Figs. 3 and 4a) at locations with a low initial dislocation density

(ρ = 2.02 × 10^{12} m^{-2}). Their load-displacement (*P-h*) curves are shown for subgrains A and B as black and red curves in Fig. 4b, respectively. They exhibit an initially purely elastic loading that can be described by the Hertzian contact theory, see the dotted light blue curve in Fig. 4b. This stage is followed by a sudden deformation event also known as initial pop-in (black arrow in Fig. 4b) at critical loads of 194 μN and 185 μN in the subgrains A and B, respectively. While initial pop-ins have been linked with different mechanisms [58], it is generally associated with the elastic-plastic transition, *i.e.*, the homogeneous nucleation of dislocations, which precedes their multiplication and motion to form pile-ups [59]. On the red load-displacement curve in Fig. 4b, this initial pop-in is followed by multiple small yield excursions highlighted by red arrows. These excursions, also known as staircase yielding, are associated with the unlocking of pre-existing pinned dislocations [47] or displacement of dislocations produced under the indenter [46,60-61].

Figures 4c-d display micrographs of the local microstructures before and after nanoindentation in subgrain A. Pre-existing threading dislocations (PEDs) are shown in Fig. 4c. Pile-ups of NIDs (blue arrow in Fig. 4d) are observed along the traces of the {111} planes. These observations are consistent with the fact that plastic deformation in the CrCoNi MEA was reported to occur by the planar glide of 1/2<110> dislocations dissociated into 1/6<112> Shockley partials on {111} planes [9]. The bright areas, enclosed by the red ellipses in Fig. 4 and subsequently in Figs. 6 and 7, corresponds to stacking faults SFs or nano-twins, which were also observed by ECCI in other materials [62-63], and were theoretically calculated by Kriaa et al.[64].

333 To differentiate PEDs and NIDs, a three-step procedure was followed. The ECC
334 micrographs before and after nanoindentation were acquired using the same
335 diffraction condition. Then, the two micrographs were superimposed to track the
336 positions of the PEDs (see GIF files in supplementary materials). Finally, new
337 dislocations that appeared after nanoindentation and formed pile-ups on {111}
338 planes were identified as NIDs. A schematic drawing of the deformed
339 microstructure in Fig. 4d is represented in Fig. 4e, where PEDs, NIDs and SFs
340 are marked in blue, yellow and red, respectively. As discussed in Section 3.1.1.,
341 the Burgers vector of threading dislocations cannot be determined using
342 extinction conditions. Consequently, the symbols ⊥ used in Figs. 4e and h and
343 subsequently in Figs. 5-7 are used to mark the positions of dislocations and do
344 not refer to their type (since there is no standard symbol for dislocations with the
345 mixed character). The PEDs remained unaltered, probably because these
346 dislocations lie outside the deformed region and do not interact with the new
347 NIDs. The pile-ups of the NIDs are visible on two sides of the indent on the traces
348 of the $(111)/(11\bar{1})$ and $(1\bar{1}1)/(1\bar{1}\bar{1})$ planes (yellow dislocations in Fig. 4e) and
349 their lengths (defined here as the distance between the outermost pile-up
350 dislocations and the center of the remnant indent) are ~0.68 μm and ~0.63 μm,
351 respectively.

352 A similar microstructural evolution was observed when nanoindentation was
353 performed in subgrain B (Figs. 4f-h). However, the average length of the pile-ups
354 on the $(111)/(11\bar{1})$ planes was longer (0.73 μm) than that in subgrain A. In
355 contrast, the mean length of the pile-ups on the $(1\bar{1}1)/(1\bar{1}\bar{1})$ planes was shorter
356 (0.55 μm) and these pile-ups are located on the opposite side of the indent-

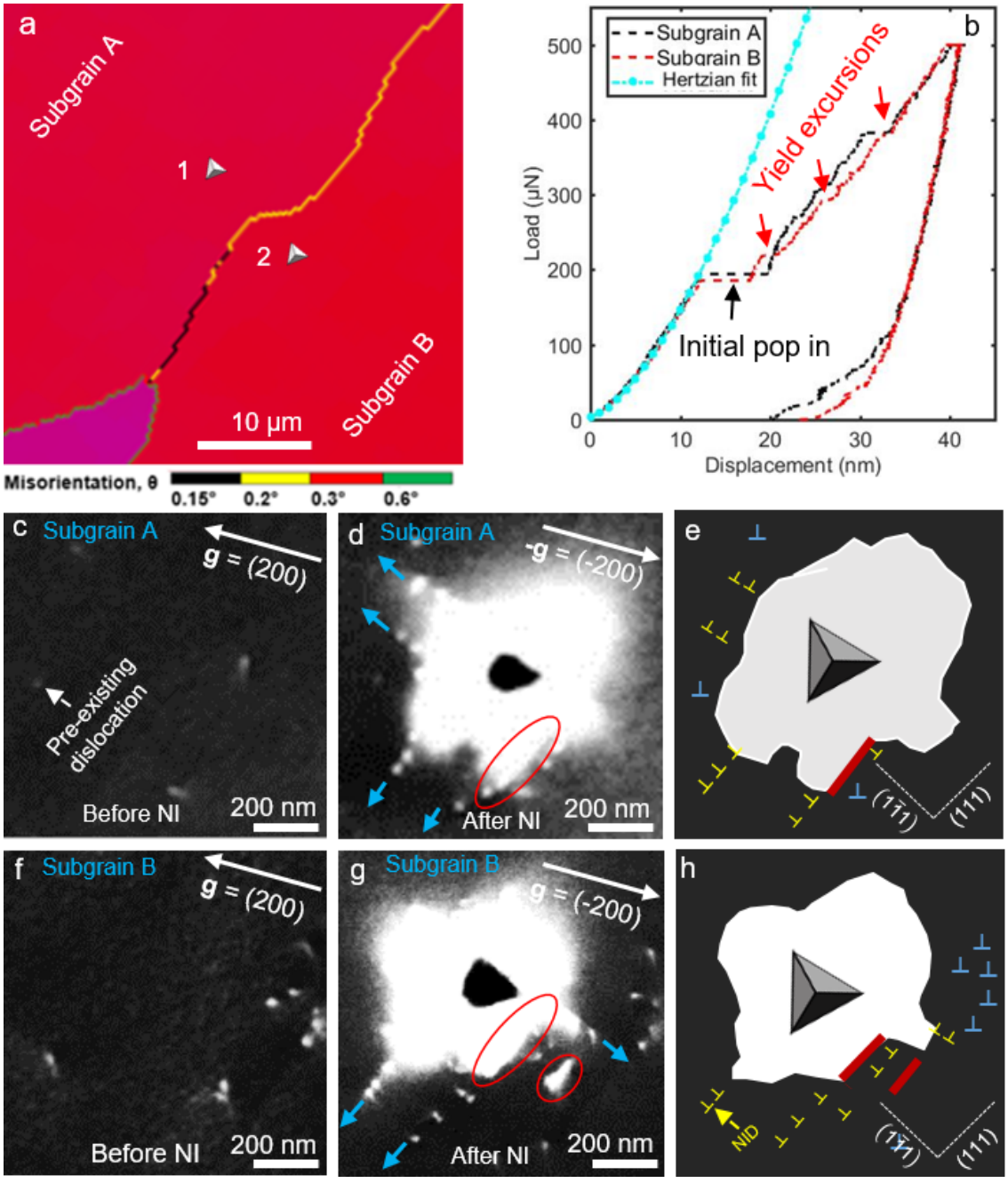

Fig. 4. (a) Positions of the indents in the subgrains A and B superimposed onto the EBSD map (indents #1 and #2 in Fig. 3a). (b) Load-displacement curves in subgrains A and B. The initial elastic loading stage follows the Hertz contact theory. (c-h) Microstructural evolution as a result of nanoindentation in regions with a low initial local dislocation density ($\rho = 2.02 \times 10^{12}$ m^{-2}). (c-d) are ECC micrographs before and after

nanoindentation in the subgrain A, respectively. (e) is a schematic of (d). (f-g) are ECC micrographs before and after deformation within subgrain B. (h) is a schematic of (g). The white dashed lines in (e and h) show the traces of the $(111)/(11\bar{1})$ and $(1\bar{1}1)/(1\bar{1}\bar{1})$ planes. The red ellipses in (d) and (g) and red thick lines in (h) and (e) mark the traces of SFs. NI and NID stand for nanoindentation and nanoindentation induced dislocation, respectively. Blue arrows in (d) and (g) show pile-ups directions. Note that the symbol ⊥ is used to mark the positions of dislocations and does not refer to their character.

-compared to subgrain A, *i.e.*, top left corner in Fig. 4d for subgrain A and bottom right corner in Fig. 4g for subgrain B. The reasons for this difference may be related to the small misorientation between subgrains A and B (compare Figs. 4c and 4f).

3.2.2. Nanoindentation on and near the LAGB

When nanoindentation is carried out on the LAGB (Fig. 5a), its corresponding load-displacement curve deviates early on from the Hertzian fit and does not show any discernable pop-in (see the black curve in Fig. 6b). This micromechanical response probably reflects the fact that, compared to homogeneous nucleation of dislocations, much lower stresses are required to induce gliding of PEDs [43]. This interpretation is supported by the microstructure that can be observed by A-ECCI around the residual indent, see Figs. 5c-d. Indeed, the NIDs around the indent (yellow dislocations in Fig. 5d) are randomly distributed and only one short dislocation pile-up is observed on one edge of the indent. This microstructural observation together with the absence of pop-ins suggests that the plasticity mostly occurred by the motion and multiplication of pre-existing LAGB dislocations.

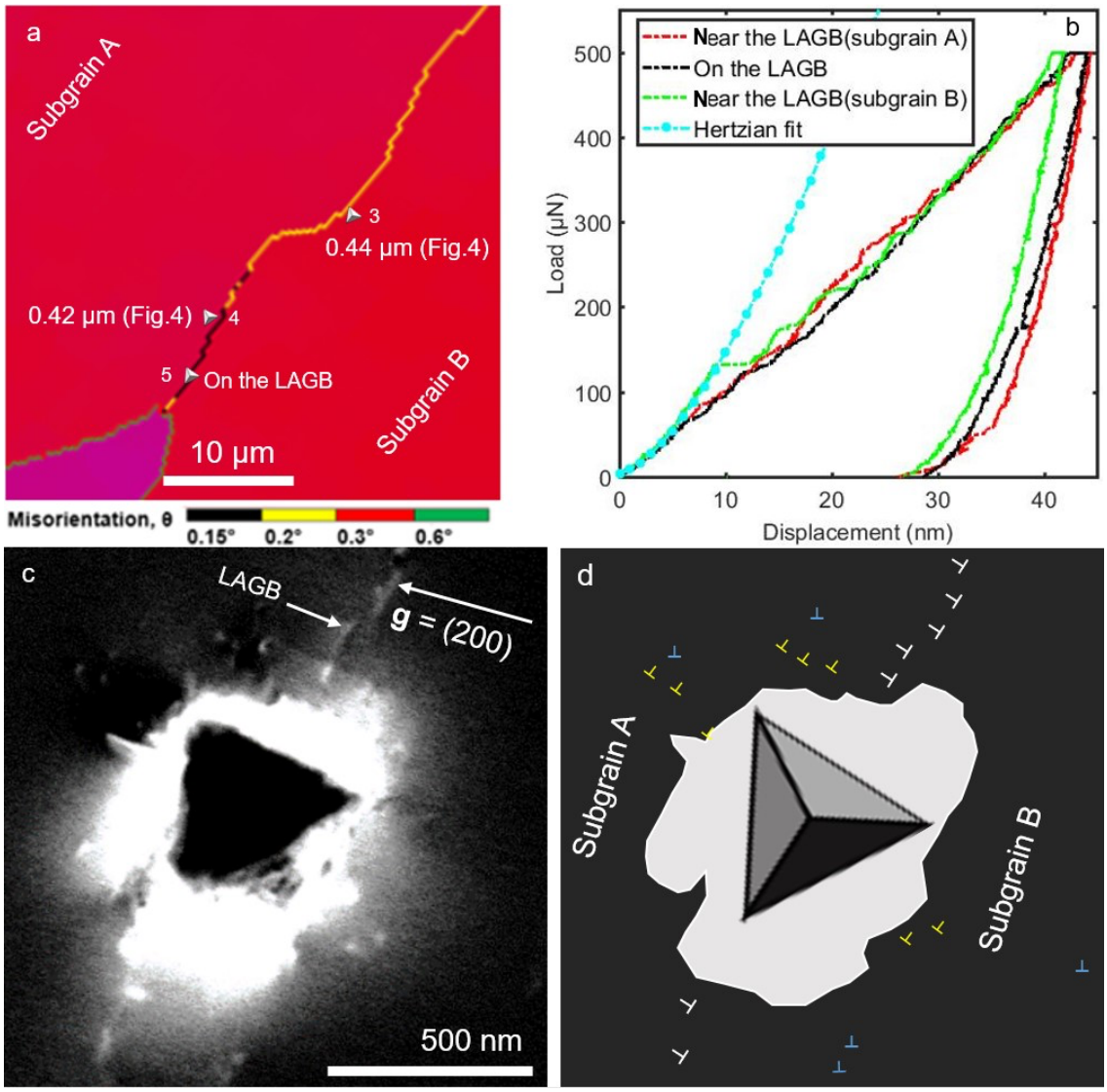

Fig. 5. (a) Positions of the indents superimposed on the subgrain orientation map. (b) Load-displacement curves of nanoindentation tests performed at the LAGB (#5), 0.42 μm (R = 0.84) from the LAGB in subgrain A (#4), and 0.44 μm (R = 0.88) in subgrain B (#3). The initial elastic loading follows the Hertz contact theory (light blue curve). (c) ECC micrograph of indent #5 performed at the LAGB and (d) corresponding schematic. Note that the symbol ⊥ is used to mark the positions of dislocations and does not refer to their character.

To investigate the interactions of dislocations with the LAGB, nanoindentation tests were performed at ~0.42 μm (R = 0.84) from the LAGB in the subgrain A

($\rho = 4.02 \times 10^{12}$ m^{-2}) and at ~0.44 µm ($R = 0.88$) from the LAGB in the subgrain B ($\rho = 4.08 \times 10^{12}$ m^{-2}), see Fig. 5a. Here, it is worth recalling that, far away from the boundary, the pile-ups on the $(1\bar{1}1)/(1\bar{1}\bar{1})$ planes in subgrains A and B were extending over 0.63 µm (Fig. 4d) and 0.55 µm (Fig. 4g), respectively.

We thus expect that nanoindentation tests #3 and #4 at distances lower than 0.5 µm ($R < 1$) from the LAGB and displayed in Figs. 3a and 5a will result in the formation of NID pile-ups that significantly interact with the LAGB and that the micromechanical responses will be affected. Interestingly, the red load-displacement curve (Fig. 5b), corresponding to the nanoindent performed in the subgrain A at $R = 0.84$, does not show an initial pop-in and behaves mechanically like the indent that was performed on the LAGB. In contrast, the green load-displacement curve in Fig. 5b, for the indent in the subgrain B at $R = 0.88$, exhibits an initial pop-in at 132 µN which is significantly lower than the mean value in this study.

The micrographs before and after nanoindentation in the subgrain A at $R = 0.84$ are presented in Figs. 6a-d. Note that the resolution in Fig. 6b is higher than in Fig. 6a due to the following reason. Since it is extremely difficult to precisely indent at a specific location, a large area along and on each side of the LAGB (25×30 µm^2) was imaged with a reasonable resolution. Such imaging is done to reduce acquisition time and avoid severe contamination of the area of interest by the electron beam *i.e.*, one has to find a compromise between acquisition time and resolution. After nanoindentation, smaller areas can be imaged again with an enhanced resolution to better visualize the deformed microstructure. The

arrangement of the dislocation pile-ups and the presence of SFs were similar to the microstructures observed for indents performed far away from the LAGB (compare Figs. 6b and 4d). The lengths of the pile-ups (yellow NIDs in Fig. 6d) are ~0.57 μm on both traces of the {111} planes and are 10-16% shorter than those for indents performed within the subgrains (far away from the LAGB). A local change of the LAGB structure is observed between LAGB dislocations 1 and 3 (dashed blue arrows in Figs. 6a-d) adjacent to the residual indent. Before nanoindentation, the LAGB dislocations 1 and 2 are clearly aligned along the green line shown in Fig. 6c. After nanoindentation, the LAGB dislocation 1 is now at the end of a nanoindentation-induced SF while the LAGB dislocation 2 shifted slightly to the right along with other LAGB dislocations between 2 and 3 as illustrated in Fig. 6d. For easier visualization of the slight motion of the LAGB dislocations near the indent, an animated superimposition of the micrographs (Figs. 6a,b) before and after nanoindentation is provided as a GIF file in Fig. S1 (Supplementary data) where two dislocations located in subgrain A far away from the indent (in the top left and top right corners of Figs. 6a,b) were used as markers for the animation. To summarize, the LAGB accommodates plastic deformation by the glide of its dislocations and this observation is consistent with the fact that no pop-ins were observed on the load-displacement curve (red in Fig. 5b). Even though the pile-ups of NIDs were not visible on the side adjacent to the LAGB, a new curved dislocation is found between the LAGB and the indent (see yellow line in Fig. 6d). This dislocation may have been stopped by the LAGB or dragged by the LAGB during its motion.

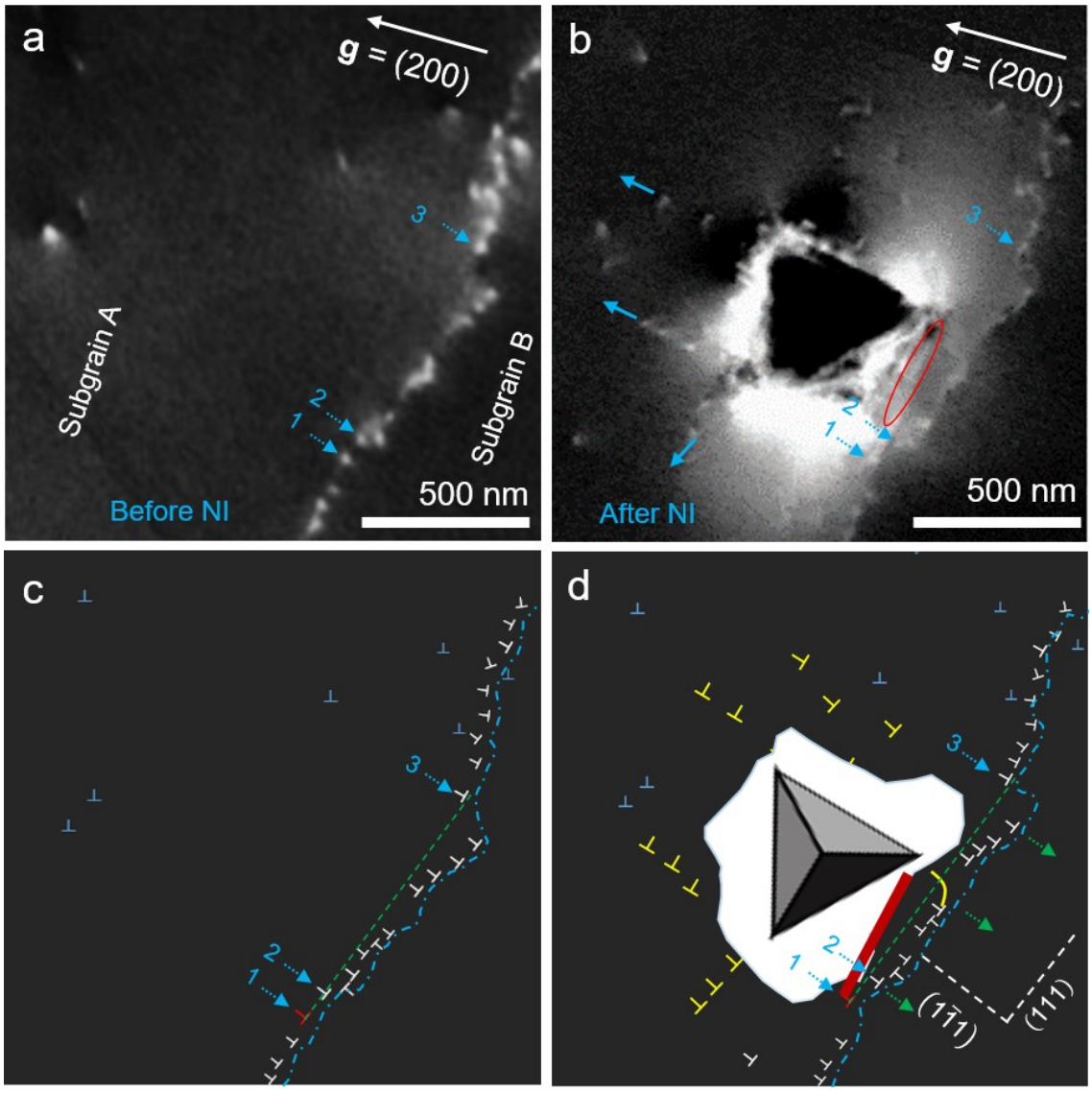

Fig. 6. (a-b) ECC micrographs before and after nanoindentation showing the evolution of the dislocation configurations in the subgrain A at 0.42 μm (R = 0.82) from the LAGB (indent #4 in Fig. 3a). (c-d) schematics of (a-b). The red ellipsis in (b) and red line in (d) show an SF. The blue arrows in (b) show directions along which the NID pile-ups extend. The blue dashed lines in (c) and (d) show the trace of the LAGB before and after deformation. The green straight lines allow to compare the positions of the LAGB dislocations 1, 2, and 3 before and after nanoindentation while the green arrows show the direction of the slight motion of LAGB dislocations. Note that the symbol ⊥ is used to mark the positions of dislocations and does not refer to their character.

Similarly, Figs. 7a-b show the microstructural evolution before and after nanoindentation for the indent performed in the subgrain B at R = 0.88. It displays pile-ups of NIDs (blue arrows in Fig. 7b) and two SFs (red ellipses in Fig. 7b) on {111} planes. The lengths of the pile-ups of NIDs are 0.63 µm and 0.57 µm on the traces of $(111)/(11\bar{1})$ and $(1\bar{1}1)/(1\bar{1}\bar{1})$ planes, respectively. Those on $(1\bar{1}1)/(1\bar{1}\bar{1})$ were expected to interact with the LAGB and a change of the dislocation structure of the LAGB was indeed observed as a result of the nanoindentation test. To better observe these evolutions, high-resolution ECC micrographs were recorded before and after nanoindentation at the location marked with a blue frame in Figs. 7a-b. These micrographs are displayed in Figs. 7c-d and their corresponding schematics showing the positions of individual dislocations are displayed in Figs. 7e-f, where dislocations of interest are numbered from one to nine. As mentioned before, please note that the resolution of Figs. 7b,d is higher than that used for Figs. 7a,c. After nanoindentation, NIDs, shown as yellow dislocations in Fig. 7f, can be observed at ~40 nm from the LAGB. These NIDs caused the rearrangement and the collective motion of the pre-existing LAGB dislocations. The rearrangement is mainly visible between the LAGB dislocations 5 and 8. Here, the dislocations form a “>” before nanoindentation that expanded after nanoindentation (compare ellipses in Figs. 7c and 7d).

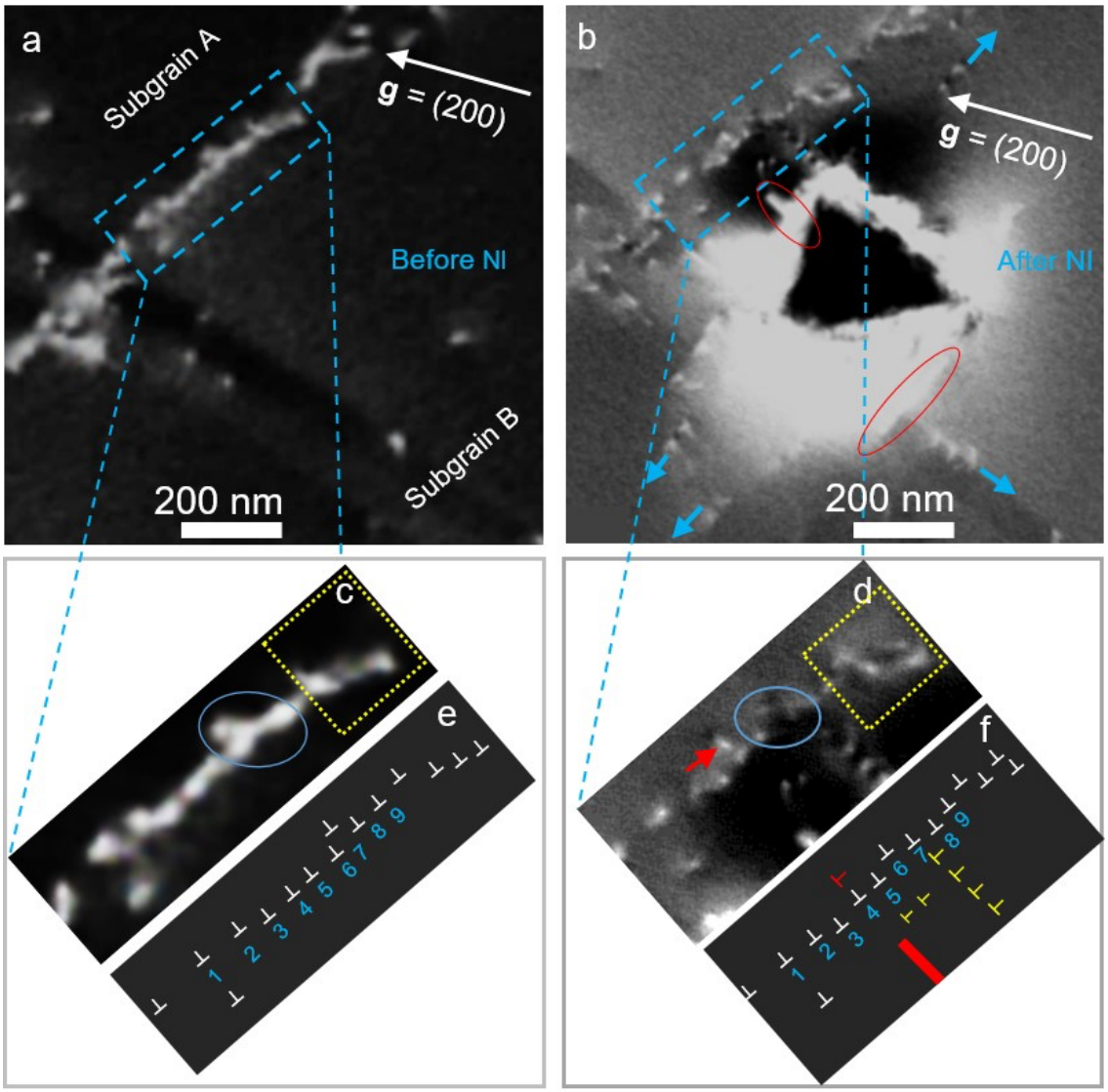

474

475 Fig. 7. Interactions between NIDs and the dislocations constituting the LAGB. (a-b) ECC
476 micrographs before and after nanoindentation, respectively (indent #3 in Fig. 3).
477 (c-d) Enlargement ECC micrograph of a portion of the LAGB before and after
478 nanoindentation and (e-f) are their corresponding schematics. The red ellipses highlight
479 SFs. Blue ellipses show dislocations that form a ">"-like shape. Note that the symbol ⊥
480 is used to mark the positions of dislocations and does not refer to their character.

481 The local collective motion of the LAGB dislocations between 1 and 9 away from
482 the residual indent (toward the subgrain A) is shown in the animated
483 superimposition of micrographs before and after nanoindentation, respectively, in

Fig. S2 (supplementary data). Note that the two dislocations located in subgrain A on the left of Figs. 7a,b were used as markers for this GIF file.

Furthermore, a new NID (highlighted by a red arrow in Fig. 7d) was observed in subgrain A (compare Figs. 7c-d and 6e-f). Since the number of dislocations remained constant in the boundary plane of the LAGB, mechanisms of decomposition, transmission, absorption, combination, or reflection of NID are not responsible for the above-mentioned dislocation generation [65-67]. Based on the position of the indents at ~0.45 μm from the LAGB and the expected pile-up size of >0.5 μm, it seems that the stress at the leading NID of the pile-up was high enough to activate a Frank-Read source in the subgrain A (note that this source cannot be resolved because it is probably smaller than the resolution limit of the A-ECCI method) or its position is deeper than the 100 nm that can be imaged by A-ECCI. Alternatively, the new dislocation could have been emitted from the LAGB. It is worth mentioning that the low misorientation angle (~0.24°) between the two subgrains ensured that the geometrical criteria for dislocation emission were satisfied [65-67].

4. Discussion

By comparing the load-displacement curves, initial pop-in loads, and dislocation microstructures for indents performed inside subgrains, near a LAGB, and on the LAGB, it is found that the studied LAGB affects the local micromechanical response and the underlying fundamental deformation mechanisms. Generally, the micromechanical responses underneath an indenter in most situations are dependent on the local microstructure such as the density of defects, their

508 configuration, and the local chemical composition [47]. At the LAGB, which
509 consists of a special configuration of dislocations, the onset of plastic deformation
510 is initiated upon contact by the motion of its dislocations because there is no need
511 to nucleate new ones. This explains the absence of an initial pop-in on the load-
512 displacement curve of indent #5 in Fig. 3. In contrast, nucleation of new
513 dislocations is needed to initiate plasticity far away from the LAGB and the
514 elastic/plastic transition on the load-displacement curve is thus marked by a
515 pronounced pop-in.

516 For the two indents at $R < 1$ in both subgrains A and B, their micromechanical
517 responses are extremely different despite being approximately at the same
518 distance from the boundary and having been placed in areas with similar
519 dislocation densities prior to nanoindentation. Such discrepancy may have been
520 caused by three reasons. First, the local organization (discrete nature, character,
521 and position of dislocations) and curvature of the LAGB are different for indents
522 #3 and #4, see Fig. 3a. Second, both indents are not symmetrical relative to the
523 LAGB plane, *i.e.*, the Berkovich indenter tip was not rotated around its axis
524 between the indents. Third, deformation mechanisms are also different as
525 evidenced by the different microstructures around the residual indents
526 (Section 3.2.2)

527 Interestingly the indents #5 and #4 performed on the LAGB and at $R = 0.84$ in
528 subgrain A, respectively, do no exhibit pop-ins (see Fig. 3) and deviate at low
529 loads from the Hertz law, even though they show different microstructure
530 evolutions during nanoindentation. For indent #4 at $R = 0.84$, the absence of
531 pop-in may be related to the sub-surface structure of the LAGB dislocations.

Indeed, if the LAGB is inclined towards the nanoindentation axis below the sample surface and deeper than the extinction depth of ECCI (~100nm), the stress field below the indenter may have interacted with the inclined dislocations of the LAGB, and plastic deformation was accommodated by the motion and multiplication of these pre-existing LAGB dislocations.

The dendritic microstructure of single crystals resulting from different processing routes and parameters was proposed to be one of the factors that may be at the origin of the significant scatter observed for the macro-mechanical CRSS of HEAs and MEAs from the Cr-Mn-Fe-Co-Ni system [18-19]. From our study, it is found that even a LAGB with a misorientation as low as 0.24° impedes the motion of dislocations, modifies the local micromechanical response and the associated deformation mechanisms. Therefore, crystal mosaicity, related to the presence of heterogeneously distributed LAGBs, which induce various misorientation angles within single crystals, is likely one of the factors responsible for the scattering of macro-mechanical CRSS values reported in the literature.

5. Conclusions

The following conclusions can be drawn from our findings. The LAGB of interest has an average misorientation of 0.24° and consists of dislocations aligned along the [001] direction with a mean spacing of ~60 nm. Besides, the elemental composition in the vicinity of this LAGB is $Cr_{35}Co_{32}Ni_{33}$ (in at.%) in a region that is ~25 µm wide while the subgrains (size: ~100 µm) have an average composition of $Cr_{30}Co_{36}Ni_{34}$. When nanoindentation tests are performed within subgrains with a maximum load of 500 µN, pile-ups of NIDs form on {111} planes around the

indents, and these pile-ups extend at least over ~0.45 μm. Therefore, when nanoindentation tests are performed at ≤ 0.5 μm ($R \leq 1$) away from the LAGB, it is expected that the heads of the dislocation pile-ups interact with the LAGB. In one case, the LAGBs blocked and absorbed the NID. In the other case, the LAGB accommodated plastic deformation through the motion and local rearrangements of its dislocations, and a new dislocation was observed after deformation on the other side of the LAGB. In terms of micromechanical response, an indent performed on the LAGB does not show an initial pop-in as the pre-existing LAGB dislocations control plasticity. Far away from the LAGB, the onset of plasticity on the load-displacement curves was marked by pop-ins. The LAGB indeed affects the local micromechanical response and fundamental deformation mechanisms as evidenced by pop-ins and microstructural evolutions. The results of this work bring new insights into dislocation/LAGB interactions and their respective micromechanical responses in metallic materials, specifically, medium- and high-entropy alloys.

Declaration of Competing Interest

The authors declare that they have no known competing financial interests or personal relationships that could have appeared to influence the work reported in this paper.

Acknowledgments

F.S. and J.F. acknowledge funding through project B7 and M.S. and G.L. through project B8 of the SFB/TR 103, supported by the German Research Foundation (DFG).

References

[1] C.G Gao, J.W. Yeh, P.K. Liaw, Y. Zhang, High entropy alloys: Fundamentals and Applications. Springer international publishing, Switzerland, 2016.

[2] J.W. Yeh, Y.L. Chen, S.J. Lin, S.K, High-entropy alloys–a new era of exploitation, Mater. Sci. Forum, 560 (2007) 1-9. https://doi.org/10.4028/www.scientific.net/MSF.560.1.

[3] Z. Wu, H. Bei, G.M. Pharr, E.P. George, Temperature dependence of the mechanical properties of equiatomic solid solution alloys with face-centered cubic crystal structures Acta Mater., 81 (2014) 428-41. https://doi.org/10.1016/j.actamat.2014.08.026.

[4] K. Ming, X. Bi, J. Wang, Strength and ductility of CrFeCoNiMo alloy with hierarchical microstructures, Int. J. Plast. 113 (2019) 255-68. https://doi.org/10.1016/j.ijplas.2018.10.005.

[5] K. Lu, A. Chauhan, M. Walter, A.S. Tirunilai, M. Schneider, G. Laplanche, J. Freudenberger, A. Kauffmann, M. Heilmaier, J. Aktaa, Superior low-cycle fatigue properties of CoCrNi compared to CoCrFeMnNi, Scr. Mater.194 (2021) 113667. https://doi.org/10.1016/j.scriptamat.2020.113667

[6] B. Gludovatz, A. Hohenwarter, K.V. Thurston, H. Bei, Z. Wu, E.P. George, R.O. Ritchie, Exceptional damage-tolerance of a medium-entropy alloy CrCoNi at cryogenic temperatures, Nat. Commun. 7 (2016) 1-8. https://doi.org/10.1038/ncomms10602.

600 [7] J.R Trife, D.E. Passoja, The effect of heat treatment on microstructure and
601 cryogenic fracture properties in 5Ni and 9Ni steel, Metall. Trans. A., 11 (1980)
602 1341–1350. https://doi.org/10.1007/BF02653488.

603 [8] S. Praveen S, H.S. Kim, High-Entropy Alloys: Potential Candidates for High-
604 Temperature Applications–An Overview Adv. Eng. Mater., 20 (2018) 1700645.
605 https://doi.org/10.1002/adem.201700645.

606 [9] G. Laplanche, A. Kostka, C. Reinhart, J. Hunfeld, G. Eggeler, E.P. George,
607 Reasons for the superior mechanical properties of medium-entropy CrCoNi
608 compared to high-entropy CrMnFeCoNi, Acta Mater., 128 (2017) 292–303.
609 https://doi.org/10.1016/j.actamat.2017.02.036.

610 [10] G. Laplanche, M. Schneider, F. Scholz, J. Frenzel, G. Eggeler, J. Schreuer,
611 Processing of a single-crystalline CrCoNi medium-entropy alloy and evolution of
612 its thermal expansion and elastic stiffness coefficients with temperature, Scr.
613 Mater., 177 (2020) 44–8. https://doi.org/10.1016/j.scriptamat.2019.09.020.

614 [11] Z. Zhang, M.M. Mao, J. Wang, B. Gludovatz, S.X. Mao, E.P. George, Q. Yu,
615 R.O. Ritchie, Nanoscale origins of the damage tolerance of the high-entropy alloy
616 CrMnFeCoNi, Nat. Commun., 6 (2015) 1-6.
617 https://doi.org/10.1038/ncomms10143.

618 [12] Z. Zhang, H. Sheng, Z. Wang, B. Gludovatz, Z. Zhang, E.P. George, Q. Yu,
619 S.X. Mao, R.O. Ritchie, Dislocation mechanisms and 3D twin architectures
620 generate exceptional strength-ductility-toughness combination in CrCoNi
621 medium-entropy alloy, Nat. Commun., 8 (2017) 1-8.
622 https://doi.org/10.1038/ncomms14390.

623 [13] M. Schneider, E.P. George, T.J. Manescau, T. Záležák, J. Hunfeld, A.
624 Dlouhý, G. Eggeler, G. Laplanche, Analysis of strengthening due to grain
625 boundaries and annealing twin boundaries in the CrCoNi medium-entropy alloy,
626 Int. J. Plast., 124 (2019) 155–69. https://doi.org/10.1016/j.ijplas.2019.08.009.

627 [14] M.C. Sangid, T. Ezaz, H. Sehitoglu, I.M. Robertson, Energy of slip
628 transmission and nucleation at grain boundaries, Acta Mater., 59 (1) (2011) 283-
629 296. https://doi.org/10.1016/j.actamat.2010.09.032.

630 [15] P. Chowdhury, H. Sehitoglu, H.J. Maier, R. Rateick, Strength prediction in
631 NiCo alloys–the role of composition and nano twins, Int. J. Plast., 79 (2016) 237-
632 258. https://doi.org/10.1016/j.ijplas.2015.07.002.

633 [16] L. Patriarca, A. Ojha, H. Sehitoglu, Y.I. Chumlyakov, Slip nucleation in single-
634 crystal CoCrFeMnNi high-entropy alloy, Scripta Mater., 112 (2016) 54-57.
635 https://doi.org/10.1016/j.scriptamat.2015.09.009

636 [17] W. Abuzaid, H. Sehitoglu, Critical resolved shear stress for slip and twin
637 nucleation in single crystalline FeNiCoCrMn high entropy alloy, Mater. Char., 129
638 (2017) 288-299. https://doi.org/10.1016/j.matchar.2017.05.014

639 [18] I.V. Kireeva, Y.I. Chumlyakov, Z.V. Pobedennaya, I.V. Kakusgausen, I
640 Karaman, Orientation dependence of twinning in single crystalline CoCrFeMnNi
641 high-entropy alloy, Mater. Sci. Eng., 705 (2017) 176-181.
642 https://doi.org/10.1016/j.msea.2017.08.065

643 [19] M. Kawamura, M. Asakura, N.L. Okamoto, K. Kishida, H. Inui, E.P. George.
644 Plastic Deformation of Single Crystals of the Equiatomic Cr− Mn− Fe− Co− Ni

645 High-Entropy Alloy in Tension and Compression from 10 K to 1273 K. Acta
646 Mater.. 203 (2020). https://doi.org/10.1016/j.actamat.2020.10.073

647 [20] B. Liu, D. Raabe, P. Eisenlohr, F. Roters, A. Arsenlis, G. Hommes,
648 Dislocation interactions and low-angle grain boundary strengthening, Acta
649 Mater., 59 (19) (2011) 7125-34. https://doi.org/10.1016/j.actamat.2011.07.067.

650 [21] B. Liu, P. Eisenlohr, F. Roters, D. Raabe, simulation of dislocation
651 penetration through a general low-angle grain boundary. Acta mater. 60 (13-14)
652 (2012) 5380-90. https://doi.org/10.1016/j.actamat.2012.05.002

653 [22] N. Verdhan N, R. Kapoor, Interaction of dislocations with low angle tilt
654 boundaries in fcc crystals. Comput. Mater. Sci., 98 (2015) 149-57.
655 https://doi.org/10.1016/j.commatsci.2014.11.006.

656 [23] R. Kapoor, N. Verdhan, Interaction of dislocation pile-up with a low-angle tilt
657 boundary: a discrete dislocation dynamics study. Philos. Mag. Lett., 97(7) (2017)
658 465-88. http://dx.doi.org/10.1080/14786435.2016.1266102

659 [24] Y. Gao, Z. Jin Z, Interactions between lattice dislocation and Lomer-type low-
660 angle grain boundary in nickel. Comput. Mater. Sci., 138 (2017) 225-35.
661 https://doi.org/10.1016/j.commatsci.2017.06.025

662 [25] W. Liu, Y. Liu, H. Sui, L. Chen, L. Yu, X. Yi, H. Duan, Dislocation-grain
663 boundary interaction in metallic materials: Competition between dislocation
664 transmission and dislocation source activation, J. Mech. Phys. Solids, 145 (2020)
665 104158. https://doi.org/10.1016/j.jmps.2020.104158

666 [26] S. Kondo, T. Mitsuma, N. Shibata, Y. Ikuhara, Direct observation of individual
667 dislocation interaction processes with grain boundaries, Sci. Adv., 11 (2016) 1–
668 8. https://doi.org/10.1126/sciadv.1501926

669 [27] T. Ohmura, A.M. Minor, E.A. Stach, J.W. Morris, dislocation–grain boundary
670 interactions in martensitic steel observed through in situ nanoindentation in a
671 transmission electron microscope. J. Mater. Res., 19 (12) (2004) 3626-32.
672 https://doi.org/10.1557/JMR.2004.0474.

673 [28] J. He, F. Scholz, O.M. Horst, P. Thome, J. Frenzel, G. Eggeler, B. Gault, On
674 the rhenium segregation at the low angle grain boundary in a single crystal Ni-
675 base superalloy, Script. Mater., 185 (2020) 88-93.
676 https://doi.org/10.1016/j.scriptamat.2020.03.063.

677 [29] S. Chen, Q. Yu, The role of low angle grain boundary in deformation of
678 titanium and its size effect, Scr. Mater., 163 (2019) 148-51.
679 https://doi.org/10.1016/j.scriptamat.2018.10.054.

680 [30] C. Ren, Z.Z. Fang, L. Xu, J.P. Ligda, J.D. Paramore, B.G. Butler, An
681 investigation of the microstructure and ductility of annealed cold-rolled tungsten,
682 Acta Mater., 162 (2019) 202-13. https://doi.org/10.1016/j.actamat.2018.10.002.

683 [31] A.C. Hall, D.J. Cook, R.A. Neiser, T.J. Roemer, D.A. Hirschfeld, The effect
684 of a simple annealing heat treatment on the mechanical properties of cold-
685 sprayed aluminum, J. Therm. Spray Technol., 15 (2) (2006) 233-8.
686 https://doi.org/10.1361/105996306X108138.

687 [32] S.R. Ahl, H. Simons, Y.B. Zhang, D. Detlefs, F. Stöhr, A.C. Jakobsen, D.J.
688 Jensen, H.F. Poulsen, Ultra-low-angle boundary networks within recrystallizing

689 grains, Scr. Mater., 139 (2017) 87-91.
690 https://doi.org/10.1016/j.scriptamat.2017.06.016.

691 [33] J.A Muñoz, R.E Bolmaro, A.M Jorge, Prediction of Generation of High- and
692 Low-Angle Grain Boundaries (HAGB and LAGB) During Severe Plastic
693 Deformation, Metall. Mater. Trans. A, 51 (2020) 4674–4684.
694 https://doi.org/10.1007/s11661-020-05873-3.

695 [34] T. Fujita, Z. Horita, T.G. Langdon, Using grain boundary engineering to
696 evaluate the diffusion characteristics in ultrafine-grained Al-Mg and Al–Zn alloys,
697 Mater. Sci. Eng. A., 371 (1-2) (2004) 241-50.
698 https://doi.org/10.1016/j.msea.2003.12.042.

699 [35] D.Song, R. Ponge, R. Kaspa, D. Raabe, Grain boundary characterization,
700 and grain size measurement in ultrafine-grained steel. Z. Metallkd., 95 (6) (2004)
701 513-7. https://doi.org/10.3139/146.017983.

702 [36] R. Carson, M. Obstalecki, M. Miller, P. Dawson, Characterizing
703 heterogeneous intragranular deformations in polycrystalline solids using
704 diffraction-based and mechanics-based metrics, Model Simul. Mat. Sci. Eng., 25
705 (5) (2007) 055008. https://doi.org/10.1088/1361-651X/aa6dc5.

706 [37] M. Zecevic, R.A. Lebensohn, R.J. McCabe, M. Knezevic, Modeling of
707 intragranular misorientation and grain fragmentation in polycrystalline materials
708 using the viscoplastic self-consistent formulation, Int. J. Plast., 109 (2018) 193-
709 211. https://doi.org/10.1016/j.ijplas.2018.06.004.

710 [38] H. Somekawa, D.A. Basha, A. Singh, Change in dominant deformation
711 mechanism of Mg alloy via grain boundary control, Mater. Sci. Eng. A., 746 (2019)
712 162-6. https://doi.org/10.1016/j.msea.2019.01.018.

713 [39] B. Yang, H. Vehoff, Dependence of nanohardness upon indentation size and
714 grain size–a local examination of the interaction between dislocations and grain
715 boundaries, Acta mater., 55(3) (2007) 849-56.
716 https://doi.org/10.1016/j.actamat.2006.09.004.

717 [40] Y.M. Soifer, A. Verdyan, M. Kazakevich, E. Rabkin, Nanohardness of copper
718 in the vicinity of grain boundaries, Scr. mater., 47 (12) (2002) 799-804.
719 https://doi.org/10.1016/S1359-6462(02)00284-1.

720 [41] W.A. Soer, J.T. De Hosson, Detection of grain-boundary resistance to slip
721 transfer using nanoindentation, Mater. Lett., 59 (24-25) (2005) 3192-5.
722 https://doi.org/10.1016/j.matlet.2005.03.075.

723 [42] M.G. Wang, A.H. Ngan, Indentation strain burst phenomenon induced by
724 grain boundaries in niobium. J. Mater. Res., 19 (8) (2004) 2478-86.
725 https://doi.org/10.1557/JMR.2004.0316

726 [43] F. Pöhl, Pop-in behavior and elastic-to-plastic transition of polycrystalline
727 pure iron during sharp nanoindentation, Sci. Rep., 9 (1) (2019) 1-12.
728 https://doi.org/10.1038/s41598-019-51644-5

729 [44] H. Mansour, J. Guyon, M. A. Crimp, N. Gey, B. Beausir, N. Maloufi. Accurate
730 electron channeling contrast analysis of dislocations in fine-grained bulk
731 materials, Scr. Mater., 84-85 (2014) 11–4.
732 https://doi.org/10.1016/j.scriptamat.2014.03.001.

733 [45] H. Kriaa, A. Guitton, N. Maloufi, Fundamental and experimental aspects of
734 diffraction for characterizing dislocations by electron channeling contrast imaging
735 in scanning electron, Sci. Rep., 17 (1) (2017) 1-8. https://doi.org/10.1038/s41598-
736 017-09756-3.

737 [46] H. Kriaa, A. Guitton, N. Maloufi, Modeling dislocation contrasts obtained by
738 accurate-Electron Channeling Contrast Imaging for characterizing deformation
739 mechanisms in bulk materials, Materials, 12 (10) (2019) 1587.
740 https://doi.org/10.3390/ma12101587.

741 [47] H. Mansour, M.A. Crimp, N. Gey, N. Maloufi, Accurate electron channeling
742 contrast analysis of a low angle sub-grain boundary, Scr. Mater., 109 (2015) 76–
743 9. https://doi.org/10.1016/j.scriptamat.2015.07.023.

744 [48] B. Chen, H. Matsuhata, K. Kumagai, T. Sekiguchi, K. Ichinoseki, H.
745 Okumura, Direct imaging and optical activities of stacking faults in 4H-SiC
746 homoepitaxial films, Int. J. Appl. Phys., 111 (5) (2012) 053513.
747 https://doi.org/10.1063/1.3691595

748 [49] J. Guyon, H. Mansour, N. Gey, M.A. Crimp, S. Chalal, N. Maloufi, Sub-micron
749 resolution selected area electron channeling patterns, Ultramicroscopy, 134
750 (2015) 34-44. https://doi.org/10.1016/j.ultramic.2014.11.004.

751 [50] P. Hallensleben, H. Schaar, P. Thome, N. Jöns, A. Jafarizadeh, I. Steinbach,
752 J. Frenzel, On the evolution of cast microstructures during the processing of
753 single crystal Ni-base superalloys using a Bridgman seed technique, Mater. Des.,
754 128 (2017) 98–111. https://doi.org/10.1016/j.matdes.2017.05.001.

[51] B. Beausir, J.J. Fundenberger, Université de Lorraine - Metz, ATEX- analysis tools for orientation maps, http://www.atex-software.eu/ (2015).

[52] S. Sagadevan, P. Murugasen P, Novel Analysis on the Influence of Tip Radius and Shape of the Nanoindenter on the Hardness of Materials, Proc. Mat. Sci., 6 (2014) 1871-8. https://doi.org/10.1016/j.mspro.2014.07.218.

[53] P. Hallensleben, F. Scholz, P. Thome, H. Schaar, I. Steinbach, G. Eggeler, J. Frenzel. On crystal mosaicity in single crystal Ni-based superalloys, Crystals, 9 (3) (2019) 149. https://doi.org/10.3390/cryst9030149.

[54] A. Vilalta-Clemente, G. Naresh-Kumar, M. Nouf-Allehiani, P. Gamarra, M.A. di Forte-Poisson, C. Trager-Cowan, A.J. Wilkinson, Cross-correlation based high-resolution electron backscatter diffraction and electron channelling contrast imaging for strain mapping and dislocation distributions in InAlN thin films. Acta Mater. 125 (2017) 125-35. https://doi.org/10.1016/j.actamat.2016.11.039

[55] D. Hull, D.J. Bacon, Introduction to dislocations, Fourth ed., Butterworth-Heinemann, Oxford, 2001.

[56] W.J. Tunstall, P.B. Hirsch, J. Steeds, Effects of surface stress relaxation on the electron microscope images of dislocations normal to thin metal foils, Philos. Mag., 9 (97) (1964) 99–119. https://doi.org/10.1080/14786436408217476.

[57] H. Kriaa, A. Guitton, N. Maloufi, Modeling dislocation contrasts obtained by accurate-Electron Channeling Contrast Imaging for characterizing deformation mechanisms in bulk materials, Materials, 12 (10) (2019) 1587. https://doi.org/10.3390/ma12101587

[58] G. Laplanche, J. Pfetzing-Micklich, G. Eggeler. Sudden stress-induced transformation events during nanoindentation of NiTi shape memory alloys, Acta mater., 78 (2014) 144-60. https://doi.org/10.1016/j.actamat.2014.05.061.

[59] Y.C. Lin, Y.J. Weng, D.J. Pen, H.C. Li, Deformation model of brittle and ductile materials under nano-indentation, Mater. Des., 30 (5) (2009) 1643-9. https://doi.org/10.1016/j.matdes.2008.07.028.

[60] A. Gouldstone, H.J. Koh, K.Y. Zeng, A.E. Giannakopoulos, S. Suresh, Discrete and continuous deformation during nanoindentation of thin films, Acta Mater., 48 (9) (2000) 2277-95. https://doi.org/10.1016/S1359-6454(00)00009-4.

[61] J.T. De Hosson, W.A. Soer, A.M. Minor, Z. Shan, E.A. Stach, S.S. Asif, O.L. Warren, In situ TEM nanoindentation and dislocation-grain boundary interactions: a tribute to David Brandon. J. Mater. Sci., 41 (23) (2006) 7704-19. https://doi.org/10.1007/s10853-006-0472-2.

[62] S. Wei, C.C. Tasan, Deformation faulting in a metastable CoCrNiW complex concentrated alloy: A case of negative intrinsic stacking fault energy? Acta Mater., 200 (2020) 992–1007. https://doi.org/10.1016/j.actamat.2020.09.056.

[63] A. Guitton, H. Kriaa, E. Bouzy, J. Guyon, N. Maloufi, A dislocation-scale characterization of the evolution of deformation microstructures around nanoindentation imprints in a TiAl alloy, Materials, 11 (2) (2018) 305. https://doi.org/10.3390/ma11020305.

[64] H. Kriaa, A. Guitton, N. Maloufi, Modelling electron channeling contrast intensity of stacking fault and twin boundary using crystal thickness effect, Materials,14 (7) (2021) 1696. https://doi.org/10.3390/ma14071696.

[65] L. Priester, Elementary Grain Boundary Deformation Mechanisms, in Grain boundaries and crystalline plasticity, ISTE Ltd, London, (2011).

[66] E. Bayerschen, A.T. McBride, B.D. Reddy, T. Böhlke, Review on slip transmission criteria in experiments and crystal plasticity models, J. Mater. Sci., 51 (5) (2016) 2243-58. https://doi.org/10.1007/s10853-015-9553-4.

[67] F. Schäfer, L. Weiter, M. Marx, C. Motz, Quantifying the grain boundary resistance against slip transfer by an experimental combination of geometric and stress approach using stage-I-fatigue cracks, Philos. Mag., 96 (32-34) (2016), 3524-3551. https://doi.org/10.1080/14786435.2016.1235289.